A plate tectonics oddity: Caterpillar-walk exhumation of subducted continental crust

C. Tirel[1], J.-P. Brun[2], E. Burov[3,4], M.J.R. Wortel[5] and S. Lebedev[1]

[1]. Dublin Institute for Advanced Studies, Geophysics Section, 5 Merrion Square, Dublin 2, Ireland. Email: celine@cp.dias.ie

[2]. Géosciences Rennes, UMR CNRS 6118 and Université de Rennes 1, Rennes, France

[3]. UPMC Sorbonne Universités, ISTEP UMR 7193, Université Pierre et Marie Curie, Paris, France.

[4]. CNRS, ISTEP, UMR 7193, F-75005, Paris, France.

[5]. Faculty of Geosciences, Tectonophysics, Utrecht University, The Netherlands

1. Numerical method, model setup and experiment description.

a) Numerical model

We use thermo-mechanical code Flamar v12 to assess the response of multi-layered visco-elasto-plastic lithosphere. The code is based on the FLAC algorithm (Cundall, 1989; Poliakov et al., 1993) and is described, following its evolution, in many previous studies (Burov and Poliakov, 2001; Burov et al., 2001; Burov et al., 2003; Burov and Guillou-Frottier, 2005; Burov and Yamato, 2008; Burov and Cloetingh, 2009). In difference from its predecessors (the above-cited references before Burov and Yamato, 2008) Flamar is thermodynamically coupled (accounts for mineralogical phase changes) and extensively relies on marker in-cell technique to trace material properties, P-T-t paths and to interpolate physical parameter fields during dynamic remeshings of the Lagrangian framework. Here we limit the description of the code to most essential features: the ability to handle (1) large strains and multiple visco-elastic-plastic rheologies including Mohr-Coulomb failure (faulting) and non-linear pressure-temperature and strain-rate dependent ductile creep; (2) stain localization and strain softening/hardening; (3) thermo-dynamic phase transitions; (4) internal heat sources; (5) free surface boundary conditions and surface processes (diffusive erosion and sedimentation).

Basic equations. Flamar has a mixed finite-difference/finite element numerical scheme, with a Cartesian coordinate frame and 2D plane strain formulation. The Lagrangian mesh is composed of quadrilateral elements subdivided into 2 couples of triangular sub-elements with tri-linear shape functions. Flamar uses a large strain fully explicit time-marching scheme. It locally solves full Newtonian equations of motion in a continuum mechanics approximation:

$$\rho \frac{D\upsilon_i}{Dt} - \frac{\partial \sigma_{ij}}{\partial x_j} = \rho g_i \qquad (1)$$

coupled with constitutive equations:

$$\frac{D\sigma}{Dt} = F\left(\sigma, \mathbf{u}, \mathbf{v}, \nabla\mathbf{u}, \nabla\mathbf{v} .. T ...\right) \qquad (2),$$

and with equations of heat transfer (where heat advection terms $\mathbf{v}\nabla T$ are included in the Lagrangian derivative *DT/D*t) and state equations:

$$\rho C_p DT/Dt - k\nabla^2 T - \sum_i^n H_i \ , \qquad (3)$$

$$\rho = f\left(P,T\right) \ . \qquad (4).$$

Here **v**,**u**, $\boldsymbol{\sigma}$, $\boldsymbol{g}$, k are the respective terms for velocity, displacement, stress, acceleration due to body forces and thermal conductivity. P is pressure (negative for compression). The terms t,ρ, C_p, T, H_i designate respectively time, density, specific heat, temperature, internal heat production, thermal expansion coefficient and isothermal compressibility. The symbol Σ means summation of various heats sources H_i. The state equation $\rho = f(P,T)$ refers to the formulation, in which phase changes are taken into account and density is computed by using free Gibbs energy minimization algorithm that evaluates the equilibrium density of constituent mineralogical phases for given P and T as well as latent heat contribution H_l to the term $\sum_i^n H_i$ ($\sum_i^n H_i = H_r + H_f + H_l + ...$). The term $\sum_i^n H_i$ also accounts for radiogenic heat H_r and frictional dissipation H_f. The terms $D\sigma/Dt$, F are the objective Jaumann stress time derivative and a functional, respectively. In the Lagrangian method, incremental displacements are added to the grid coordinates allowing the mesh to move and deform with the material. This allows for the solution of large-strain problems while using locally the small-strain formulation: on each time step the solution is obtained in local coordinates, which are then updated in a large-strain mode.

Solution of (1) provides velocities at mesh points used for computation of element strains and of heat advection $\mathbf{v}\nabla T$. These strains are used to calculate element stresses and equivalent forces used to compute velocities for the next time step. Due to the explicit approach, there are no convergence issues in case of non-linear rheologies. The algorithm automatically checks and adopts the internal time step using Courant's criterion of stability. Once Courant's criterion is satisfied, physical instabilities are treated in correct way since in this case the algorithm cannot miss forks in physical processes.

Explicit elastic-viscous-plastic rheology. We use common serial Maxwell-type solid, in which the total strain increment in each numeric element is defined by a sum of elastic, viscous and brittle strain increments. In contrast to fluid dynamic approaches, where non-viscous rheological terms are simulated using pseudo-plastic and pseudo-elastic viscous terms (Solomatov and Moresi, 2000; Bercovici and Ricard, 2001), Flamar explicitly treats all rheological three terms. The parameters of elastic-ductile-plastic rheology laws for crust and mantle are derived from rock mechanics data (Supplementary Table1).

Plastic (brittle) behavior. The brittle behaviour of rocks is described by Byerlee's law (Byerlee, 1978), which corresponds to a Mohr-Coulomb material with friction angle $\phi = 30°$ and cohesion $|C_0| < 20$ MPa:

$$|\tau| = C_0 - \sigma_n \tan\phi\,, \tag{5}$$

where σ_n is normal stress $\sigma_n = \frac{1}{3}\sigma_I + \sigma_{II}^{dev} \sin\phi$, $\frac{1}{3}\sigma_I = P$ is the effective pressure (negative for compression), σ_{II}^{dev} is the second invariant of deviatoric stress, or effective shear stress. The condition of the transition to brittle deformation (function rupture f) reads as: $f = \sigma_{II}^{dev} + P \sin\phi - C_0 \cos\phi = 0$ and $\partial f/\partial t = 0$. In terms of principal stresses, the equivalent of the yield criterion (6) reads as:

$$\sigma_1 - \sigma_3 = - \sin\phi\,(\sigma_1 + \sigma_3 - 2C_0/\tan\phi) \tag{6}$$

Elastic behaviour. Elastic behaviour is described by the linear Hooke's law:

$$\sigma_{ij} = \lambda\varepsilon_{kk}\delta_{ij} + 2G\varepsilon_{ij}, \qquad (7)$$

where λ and G are Lame's constants. Repeating indexes mean summation and d is the Kronecker's operator.

Viscous (ductile) behaviour. Within deep lithosphere and underlying mantle regions, creeping flow is highly dependent on temperature and is non-linear non-Newtonian since the effective viscosity also varies as function of differential stress (Kirby and Kronenberg, 1987; Turcotte and Schubert, 2002):

$$\dot{\varepsilon}^{d} = A\,(\sigma_1 - \sigma_3)^{\,n} \exp(-Q\,R^{-1}T^{-1}), \qquad (8)$$

where $\dot{\varepsilon}^{d}$ is effective shear strain rate, A is a material constant, n is the power-law exponent, $Q = Ea + PV$ is the activation enthalpy, E_a is activation energy, V is activation volume, P is pressure, R is the universal gas constant, T is temperature in K, σ_1 and σ_3 are the principal stresses. The effective viscosity μ_{eff} for this law is defined as:

$$\mu_{eff} = \dot{\varepsilon}^{\,(1-n)/n} A^{-1/n} \exp(Q\,(nRT)^{-1}). \qquad (9)$$

For non-uniaxial deformation, the law (9) is converted to a triaxial form, using the invariant of strain rate and geometrical proportionality factors:

$$\mu_{eff} = \dot{\varepsilon}^{d}_{II}{}^{(1-n)/n} (A^{*})^{-1/n} \exp(Q\,(nRT)^{-1}), \qquad (10)$$

where $\dot{\varepsilon}^{d}_{II} = (\mathrm{Inv}_{II}(\dot{\varepsilon}_{ij}))^{1/2}$ and $A^{*} = \frac{1}{2}A\cdot 3^{(n+1)/2}$. The parameters A, n, Q are the experimentally determined material constants (Supplementary Table 1). Using olivine flow parameters, we verify that the predicted effective viscosity at lithosphere asthenosphere boundary is 10^{19}– 5 x 10^{19} Pa s matching post-glacial rebound data

(Turcotte and Schubert, 2002). Due to temperature dependence of the effective viscosity, the viscosity decreases from 10^{25}-10^{27} Pa s to asthenospheric values of 10^{19} Pa s in the depth interval 0-152 km. Within the adiabatic temperature interval in the convective upper mantle (152 km –700km), the dislocation flow law (9) is replaced by a nearly Newtonian diffusion creep. We also use Peierl's stress limiter that limits deviatoric stresses in mantle (*7*) assuming Peierl's stress of 5GPa.

b) Initial and boundary conditions

The model geometry (Supplementary Fig. 1) comprises a rectangular box (2000 x 700 km) with variable spatial resolution: 85 x 115 quadrilateral bilinear elements (4 km x 4 km) for the first 340 km depth and 36 x 115 quadrilateral bilinear elements (10 km x 4 km) below 300 km depth. Each element of the numerical grid is assigned its specific material phase defined as a subset of physical parameters of the corresponding material: density, thermal and rheology parameters (Supplementary Table 1). The initial geometry assumes an already initiated oceanic subduction, with the subducting slab reaching down to 272-km depth. Two blocks of continental crust are embedded in the subducting plate, fated to be accreted to the overriding plate in the course of the ongoing subduction. These continental blocks are 400 km wide and with 44-km thick crust (representing characteristic dimensions of micro-continental terrains and reconstructed volumes of accreted metamorphic rocks (Brun and Faccenna, 2008; Jolivet and Brun, 2010)). The two continental blocks are at 150 km away from each other (following those structural reconstructions), with oceanic lithosphere in between. The continental crust is assumed to be homogeneous and of quartzite-type composition (Ranalli and Murphy, 1987), with a density of 2800 kg m^{-3}; sediments (Kronenberg and Tullis, 1984) have a density of 2400 kg m^{-3}. Oceanic crust is represented by gabbro basalt and crust-mantle interface – by serpentinite (Hilairet, 2007), both with a density of 2900 kg m^{-3} and the subducting mantle lithosphere is represented by olivine (Brace and Kohlstedt, 1980) with density of 3350 kg m^{-3}. The mechanical boundary conditions assigned on the four sides of the box are: at the left and right side are fixed horizontally; at the bottom: hydrostatic pressure with free slip in all directions; the upper surface is explicitly free (free stress and free slip/displacement condition in all directions), with moderate diffusion surface erosion (k_e = 500 m^2/yr, see e.g. Burov and Yamato, 2008). The bottom is pliable Winkler basement (= hydrostatic condition). A bottom layer is introduced with a viscosity and a density higher than for the subducting slab, to simulate pressure-induced viscosity growth toward the transition at 660 km depth and to avoid extreme deformation of the bottom of the box when the slab reaches it. Plastic and viscous materials soften with accumulated strain through a decrease of the angle of friction and cohesion and decrease in viscosity, respectively (Supplementary Table 1).

c) Thermal structure of the lithosphere

The thermal structure is one of the key parameters defining the mechanical strength and buoyancy of the lithosphere. In this model, the thermal base of the lithosphere (1330°C) is placed at 200 km depth corresponding to old oceanic lithosphere approaching subduction zone (Schubert et al., 2001). The surface temperature is fixed at 0°C and zero heat flow (no heat exchanges with the surrounding region) is set as the lateral thermal boundary condition. The initial background geotherm for the mantle lithosphere system is obtained by joining the lithospheric and deep mantle adiabatic geotherms (approx. 0.3°C/km, Sleep, 2003). Fixed temperature of 1600°C is used as bottom boundary condition at 700 km depth. The initial geotherms in the lithosphere are age-deoendant (Parsons and Sclater, 1977; Burov and Diament, 1992; 1995). Moreover, the initial geotherm within the subducting slab is represented by an oceanic lithosphere with a 0°C at surface and 1330°C at the base following the slab approximation described in Burov and Diament (1995) for an old oceanic geotherm.

2. Deformation of the blocks in slab rollback process

Supplementary Fig. 2a represent step-by-step evolution of the central part of the model. Additional passive markers (color circles) allow for tracing of key parts of the model (see also Supplementary Fig 3). Supplementary Fig. 2b shows the step-by-step evolution of the strain rate field, and instantaneous deformation at each time step. The first phase of evolution is characterized by the accretion of the block 1 underthrusted below the accretionary wedge and oceanic suture zone. The consequence of this accretion is the burial of a part of continental block, that remains cold, and the increase of the slab dip due to the negative buoyancy of the buried continental crust. The ongoing thrusting is responsible for splitting of the continental block on two parts, its left part dragged under its right part along the new major thrust. When this part is buried it pushes up the previously buried part of the block, forcing it to the surface. After that the first major thrust is changed in a normal detachment to accommodate the exhumation of the right part of the first block. The oceanic subduction that continues after the accretion of block 1, while this latter is still partly attached to the subducted slab, provokes a rotation of the entire block still at the favor of the slip of the normal detachment. As result of this rotation, exhumed crustal structure is inversed, with lower crust exposed to the surface. When the oceanic subduction advances enough to decouple the block 1 from its subducting mantle part, the dip of the slab decreases and the block is no longer undergoing rotation. The fully decoupled block 1 now belongs to the overriding plate. The change of the dip of the slab combined with the acceleration of the slab retreat result in the ascent of the asthenosphere below the right tip of the block. When the block 2 arrives at the trench, the dip of the slab increases, leading to the rising of the asthenosphere below the entire first block. The warming of the block 1 can be seen on the P-T-t paths in Supplementary Fig 3. The association between the extension and the vigorous warming of the first continental block results in a metamorphic core complex mode of exhumation. This deformation mode, based on a crustal flow, enables a considerable amount of stretching while the Moho stays practically flat. The extension is mostly localized in this part because the ductile potential is high. The accretion of the block 2 occurs in the same way than the first one. The only difference is that the left tip of the block stays somehow connected to the trench, and is not completely decoupled from the slab as it is for the block 1.

3. Pressure-temperature-time paths

Supplementary Fig. 3 shows the final structure with several colored markers located both in blocks 1 and 2. Their PTt paths are shown in Supplementary Figure 3b. The PTt paths of two blocks show different patterns that we can qualify as “cold” or “hot”. The “hot” paths of the block 1 are the blue and the pink one, yellow for the block 2. They are characterized by an effective burial to ~2 to 3GPa followed by a rapid cold exhumation and then a strong increase of temperature related to the detachment of the blocks from the slab and the consequent asthenospheric warming. The “cold” paths (all the other ones) are characterized by an effective burial to ~2 to 3GPa followed by a rapid cold exhumation.

4. Reference experiment with laterally homogeneous lithosphere (no continental blocks)

Supplementary Fig. 4 shows several steps of an experiment without the continental blocks in the subducting slab. As for the experiments with heterogeneous lithosphere, slab retreat starts immediately as well as the extensional deformation in the overriding crust. A part of the continental lithosphere that forms the overriding plate is extremely stretched to accommodate the extension due to the slab rollback (from 0 to 42.5 Myr). Then high slab break-off occurs, stopping the subduction process as well as the extensional deformation in the overriding plate (70.3 Myr). This experiments shows that in the absence of structural heterogeneities, the subduction, roll-back and exhumation are only one-staged progressive, and the roll-back has a much smaller amplitude.

Supplementary references:

Bercovici, D., Ricard, Y., and Schubert, G., 2001, A two-phase model for compaction and damage, part 3: application to shear localization and plate boundary formation: Journal of Geophysical Research, v. 106, p. 8925-8939.

Brace, W.F., and Kohlstedt, D.L., 1980, Limits on Lithospheric Stress Imposed by Laboratory Experiments: Journal of Geophysical Research, v. 85, p. 6248-6252.

Burov, E., and Cloetingh, S., 2009, Controls of mantle plumes and lithospheric folding on modes of intra-plate continental tectonics: differences and similarities: Geophysical Journal International, v. 178, p. 1691-1722.

Burov, E., and Guillou-Frottier, L., 2005, The plume head-continental lithosphere interaction using a tectonically realistic formulation for the lithosphere: Geophysical Journal International, v. 161, p. 469-490.

Burov, E., Jaupart, C., and Guillou-Frottier, L., 2003, Ascent and emplacement of magma bodies: Journal of Geophysical Research, v. 108, p. 2177.

Burov, E., and Poliakov, A., 2001, Erosion and rheology controls on synrift and postrift evolution; verifying old and new ideas using a fully coupled numerical model: Journal of Geophysical Research, v. 106, p. 16,461-16,481.

Burov, E.B., and Diament, M., 1992, Flexure of the continental lithosphere with multilayered rheology: Geophysical Journal International, v. 109, p. 449-468.

,Äî, 1995, The effective elastic thickness (Te) of continental lithosphere: What does it really means?: Journal of Geophysical Research, v. 100, p. 3905-3927.

Byerlee, J.D., 1978, Friction of rocks: Pure and Applied Geophysics, v. 116, p. 615-626.

Cundall, P.A., 1989, Numerical experiments on localization in frictional materials: Ingenieur-Archiv., v. 59, p. 148-159.

Hilairet, N., Reynard, B., Wang, Y., Daniel, I., Merkel, S., Nishiyama, N., and Petitgirard, S., 2007, High-Pressure Creep of Serpentine, Interseismic Deformation, and Initiation of Subduction: Science, v. 318, p. 1910-1913.

Kirby, S.H., and Kronenberg, A.K., 1987, Rheology of the Lithosphere: Selected Topics: Reviews of Geophysics, v. 25, p. 1219-1244.

Kronenberg, A.K., and Tullis, J., 1984, Flow strengths of quartz aggregates: grain size and presure effects due to hydrolytic weakening: Journal of Geophysical Research, v. 89, p. 4298-4312.

Parsons, B., and Sclater, J.G., 1977, An analysis of the variation of ocean floor bathymetry and heatflow with age Journal of Geophysical Research, v. 82, p. 803-827.

Poliakov, A.N.B., Cundall, P., Podlachikov, Y., and Laykhovsky, V., 1993, An explicit inertial method for the simulation of visco-elastic flow: an evaluation of elastic effects on diapiric flow in two and three-layers models, in Stone, D.B., and Runcorn, S.K., eds., Flow and Creep in the Solar System: Observations, Modelling and Theory, Dynamic Modelling and Flow in the Earth and Planets Series: Holland, Kluwer, p. 175-195.

Ranalli, G., 1995, Rheology of the Earth: London, Chapman and Hall, 413 p.

Ranalli, G., and Murphy, D.C., 1987, Rheological stratification of the lithosphere: Tectonophysics, v. 132, p. 281-295.

Schubert, G., Turcotte, D.L., and Olson, P., 2001, Mantle convection in the Earth and planets: Cambridge, Cambridge University Press, 940 p.

Sleep, N.H., 2003, Survival of Archean cratonal lithosphere: Journal of Geophysical Research, v. 108, p. 2302.

Solomatov, V.S., and Moresi, L.N., 2000, Scaling of time-dependant stagnant lid convections;application to small-scale convection on Earth and other terrestrial planets: Journal of Geophysical Research, v. 105, p. 21795-21817.

Turcotte, D.L., and Schubert, G., 2002, Geodynamics: Cambridge, Cambridge University Press, 456 p.

Supplementary figures, table and movie captions:

Supplementary Fig. DR1: a) Initial and boundary conditions of the experiment, b) initial thermal conditions

Supplementary Fig. DR2: a) Zoom to the uppermost part of the plate contact zone in the model, with selected passive markers (coloured circles), b) strain rate distributions in the of the upper part of the experiment (showing localization of deformation, in particular crustal detachments). This figure is spread on to three sheets. Figure shows step-by-step evolution of the central part of the model where two embedded continental crustal blocks first subduct and then get exhumed to the surface, with the material of the second block sliding below and behind the exhumed preceding block. Delamination of the crustal blocks has a major impact on the evolution of the subduction zone and, in the particular, on slab roll-back and back-arc extension. On their way to the surface blocs undergo reversing rotation, just like a caterpillar bent, resulting in inversion of the crustal structure at surface. At surface, both crustal blocks stretch laterally forming large scale metamorphic terrain structurally resembling structural reconstructions of the Aegean realm (Fig. 1)

Supplementary Fig. DR3: a) Final structure of the experiment with the final position of the colored markers shown in Fig. S2, b) pressure-temperature paths through time (PTt) of the markers of block 1, c) pressure-temperature paths through time (PTt) of the markers of block 2.

Supplementary Fig. DR4: Several snapshots of the experiment with laterally homogeneous lithosphere ,i.e. without continental blocks in the subducting slab.

Supplementary Table DR1: Parameters of the experiments.

Supplementary Movie DR1: This movie shows the evolution of the structural pattern of the experiment.

Supplementary Table DR 1: Numerical parameters

		Continental crust	Sediments	Oceanic crust	Lithospheric mantle	Mantle	660km boundary
		Quartzite dry[1]	Quartzite wet[2]	Serpentinite[3]	Olivine[4]	Olivine[4]	Olivine[4]
Viscosity parameters	n	2.4	2.7	3.8	3	3	3
	A, $MPa^{-n}.s^{-1}$	6.3×10^{-6}	2.18×10^{-6}	4.5×10^{-15}	7×10^{4}	7×10^{4}	7×10^{4}
	E, $kJ.mol^{-1}$	156	120	89	520	520	520
Minimum viscosity					10^{21}		10^{25}
Density $kg.m^{-3}$		2700 (3350*)	2400	2900 (3350**)	3350	3320-3330	3360
Elastic parameters	λ, Pa	3×10^{10}	3×10^{10}	1×10^{10}	3×10^{10}	1×10^{10}	4×10^{10}
	μ, Pa	3×10^{10}	3×10^{10}	1×10^{10}	3×10^{10}	1×10^{10}	4×10^{10}
Cohesion, Pa		20 to 0	20 to 0	20 to 0	20	20	300
Frictional angle, °		10 to 2	10 to 2	10 to 2	30	30	2
Thermal conductivity, $W.m^{-1}.K^{-1}$		2.5	2.5	3.5	3.5	3.5	3.5
Specific heat Cp, $J.kg^{-1}.K^{-1}$		1×10^{3}	1×10^{3}				
Internal heat production at surface, hs, $W.kg^{-1}$		1×10^{-9}	1×10^{-9}				
Production decay depth, hr, km		10	10				

[1] from Ranalli and Murphy 1987, [2] from Kronenberg and Tullis, 1984, [3] from Hilairet et al, 2007,
[4] from Brace and Kohlstedt, 1980

* change of density when pressure > 5×10^{9} and temperature > 550°C

** deep oceanic crust at the onset of experiments

a)

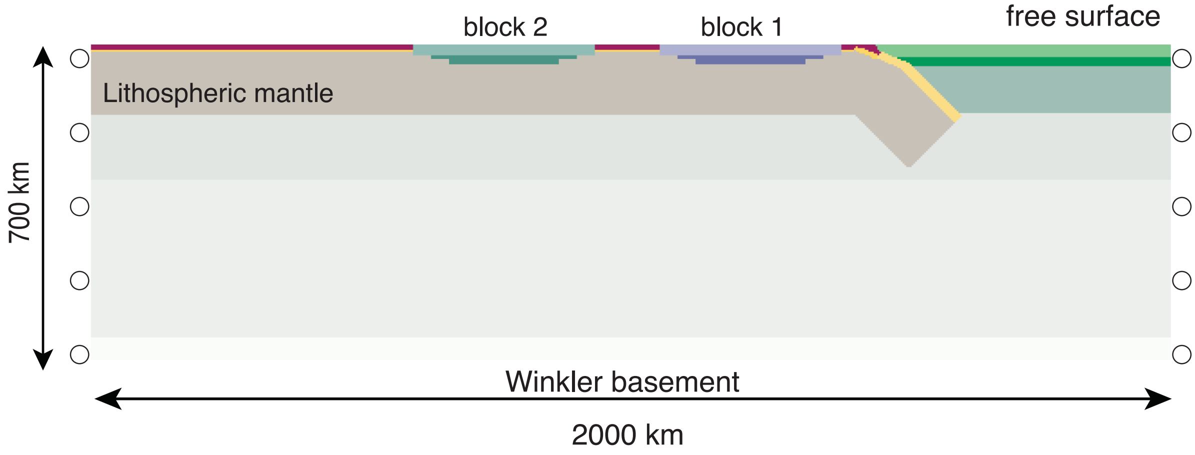

b)

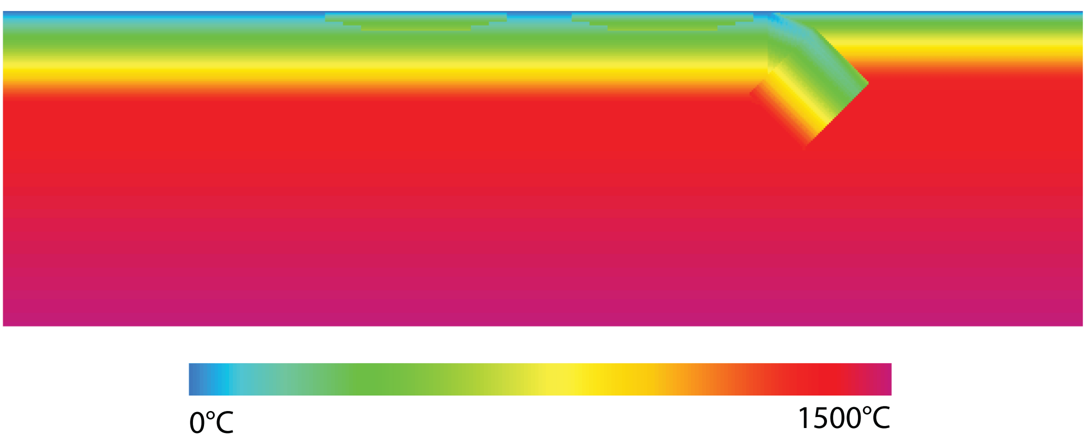

Supplementary Figure 1: a) Initial and boundary conditions of the experiment, b) initial thermal conditions

Figure DR1

a)

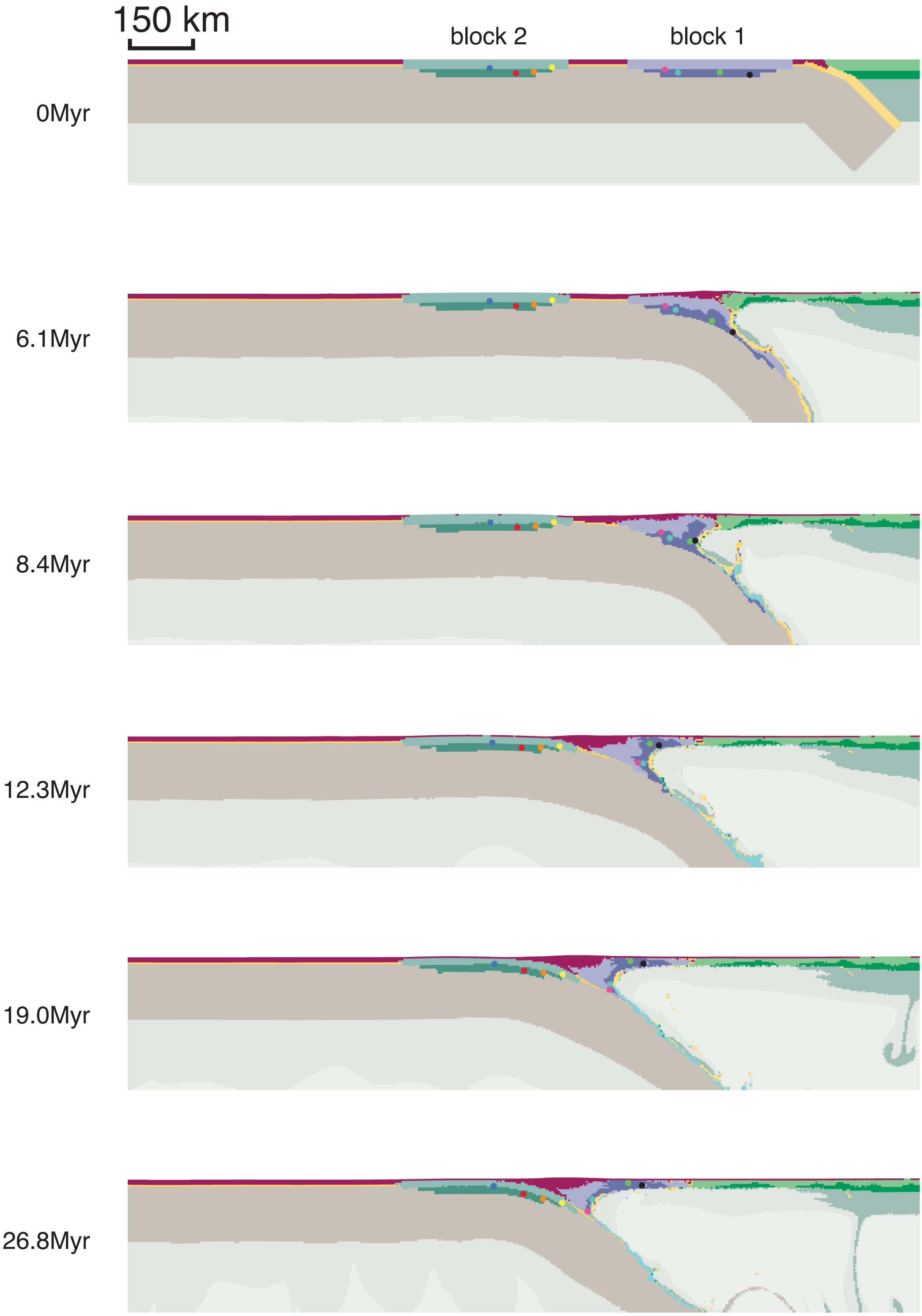

Figure DR2

a)

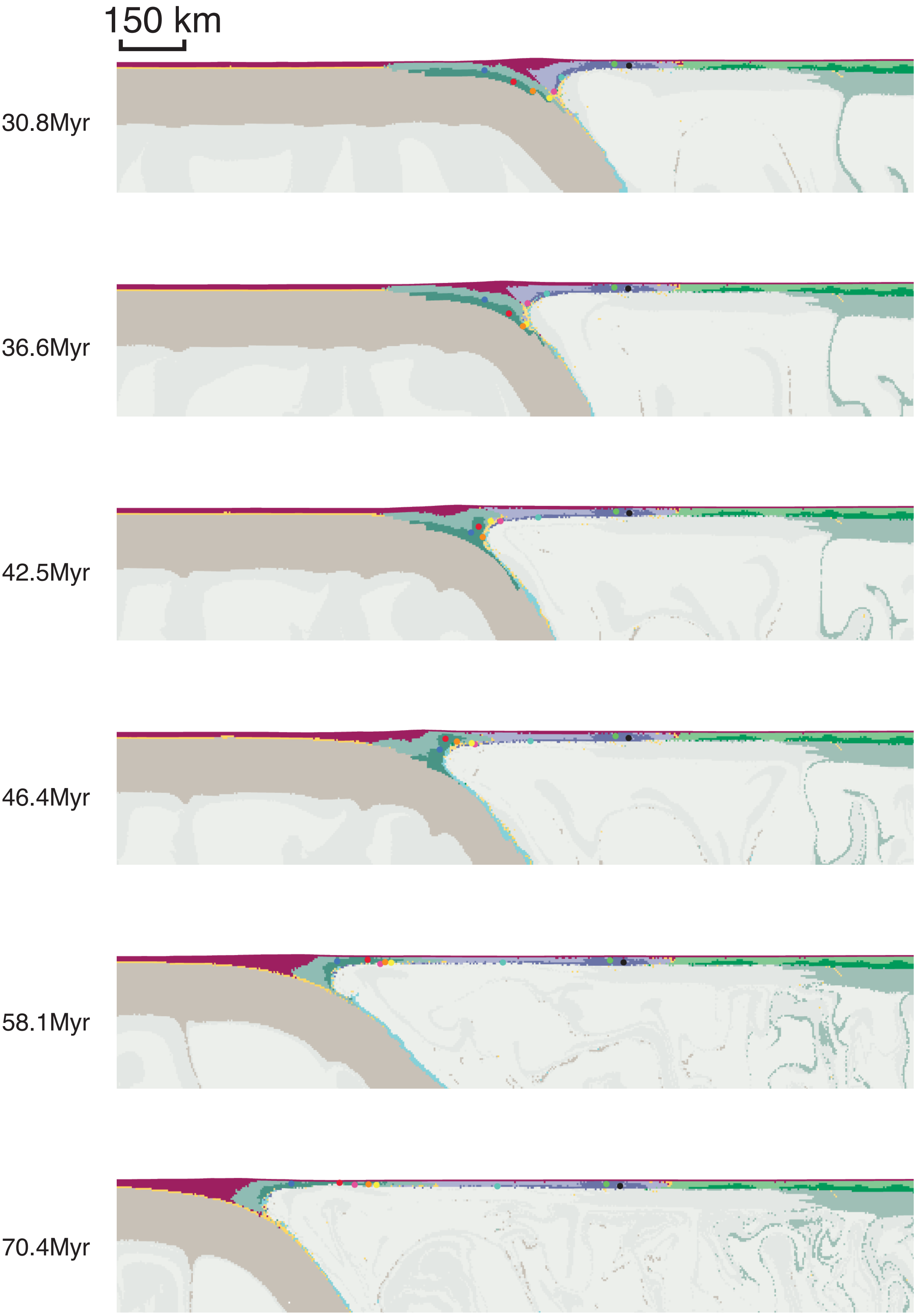

Figure DR2 (cont)

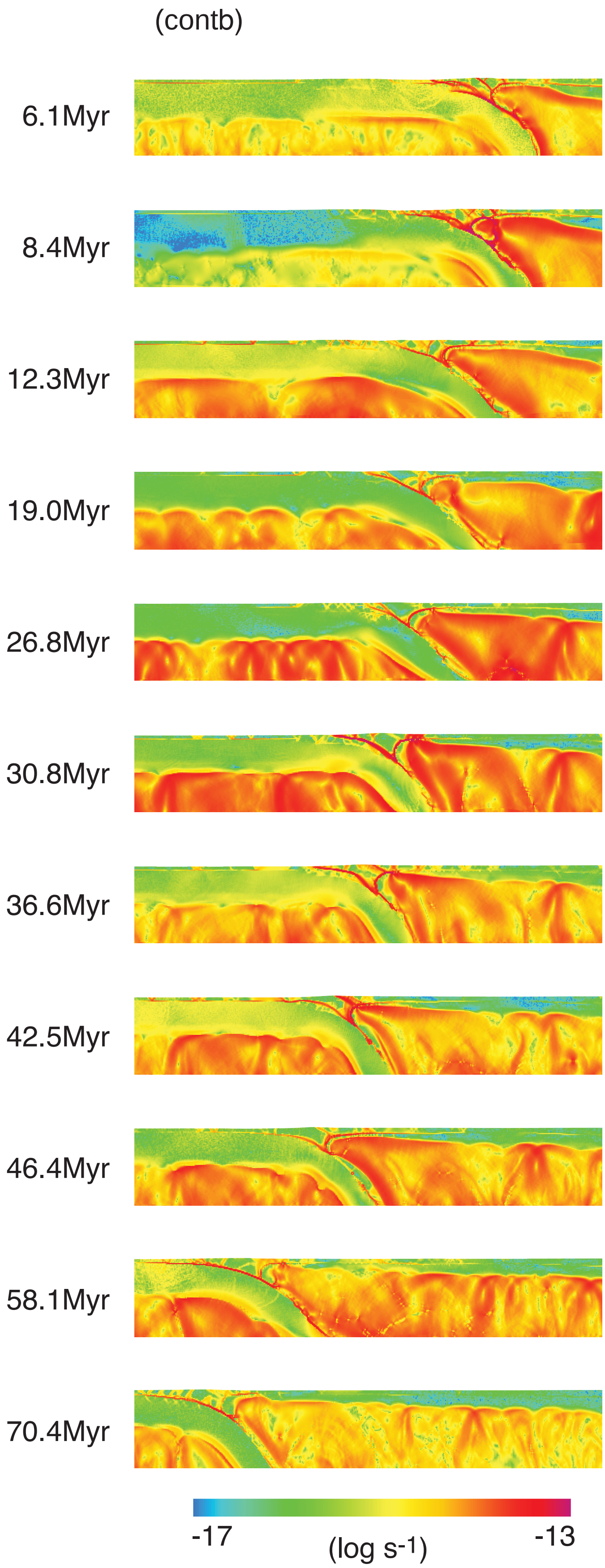

Supplementary Figure DR2: a) structure of a upper part of the experiment with some markers, b) strain rate of the upper part of the experiment. The figure is spread on three sheets.

Figure DR2 (cont)

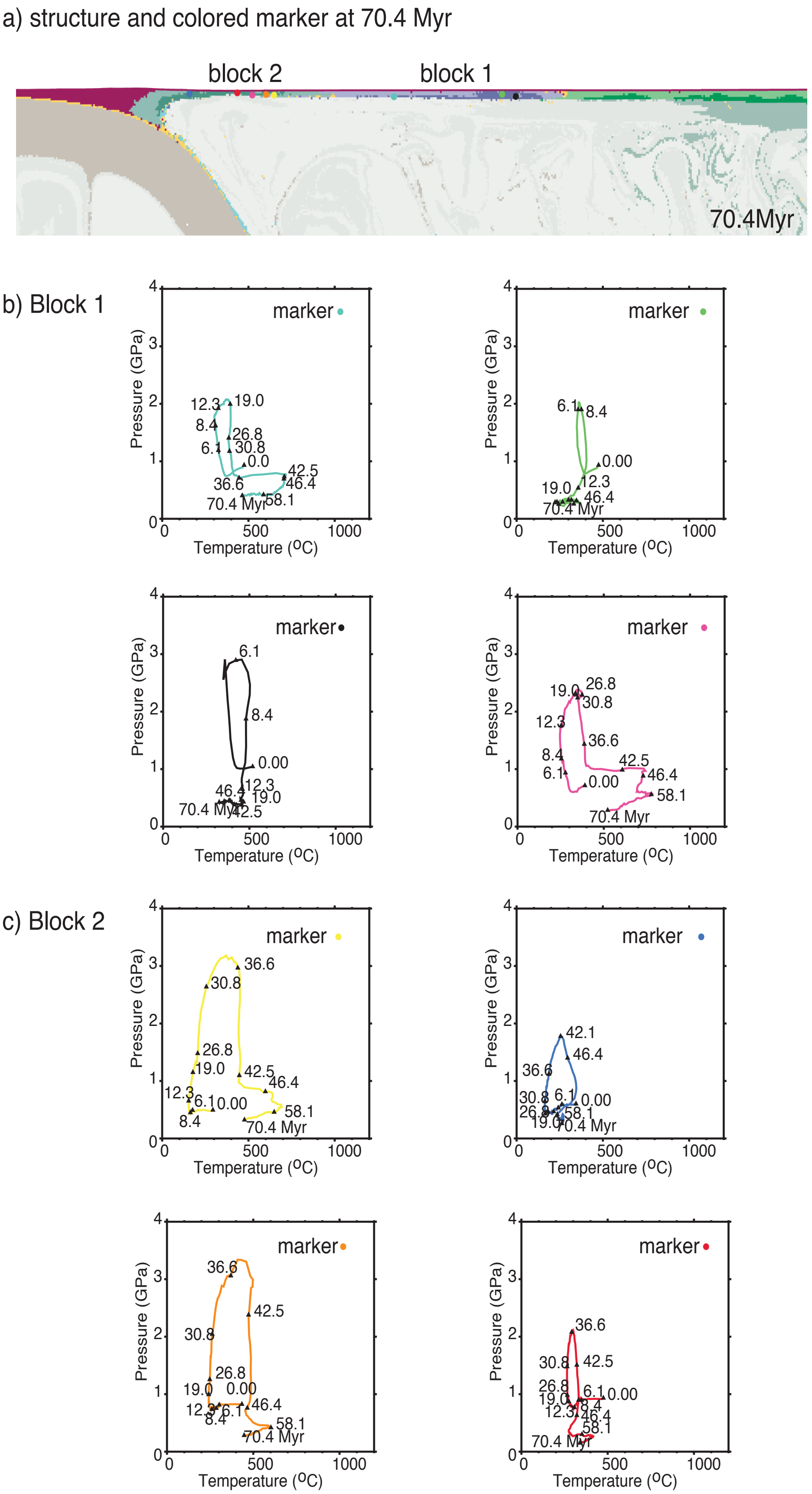

Supplementary Figure DR3: a) Final structure of the experiment with the position of the colored markers also presented in Supplementary Figure 2,
b) pressure-temperature paths through time of the markers of block 1,
c) pressure-temperature paths through time of the markers of block 2.

Figure DR3

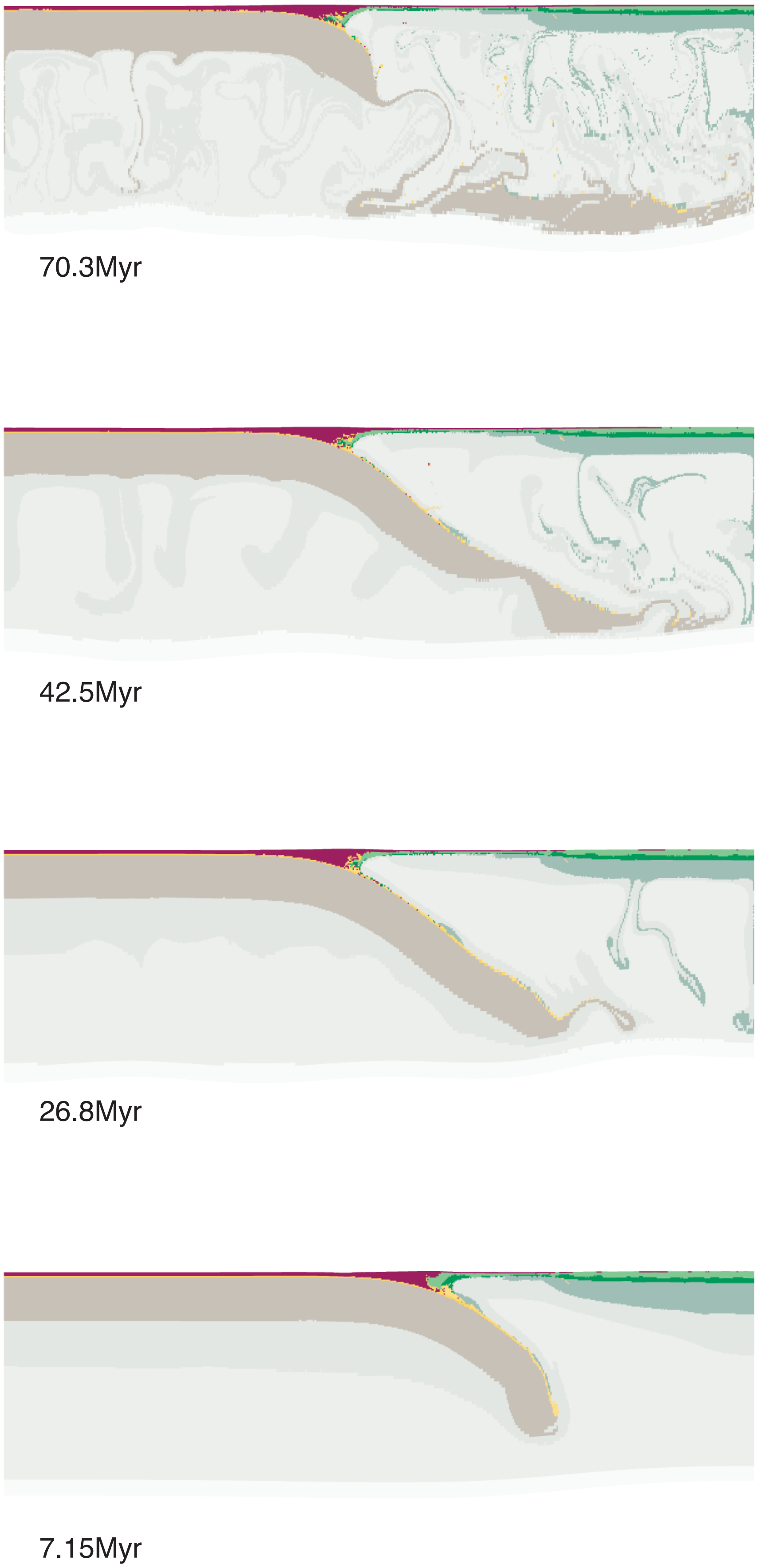

Supplementary Figure DR4: Snapshots of an experiment without any microcontinent.

Figure DR4